

SCIENTIFIC REPORTS

OPEN

Crystalline Ni₃C as both carbon source and catalyst for graphene nucleation: a QM/MD study

Received: 10 February 2015

Accepted: 17 June 2015

Published: 14 July 2015

Menggai Jiao^{1,2}, Kai Li¹, Wei Guan¹, Ying Wang¹, Zhijian Wu¹, Alister Page³ & Keiji Morokuma⁴

Graphene nucleation from crystalline Ni₃C has been investigated using quantum chemical molecular dynamics (QM/MD) simulations based on the self-consistent-charge density-functional tight-binding (SCC-DFTB) method. It was observed that the lattice of Ni₃C was quickly relaxed upon thermal annealing at high temperature, resulting in an amorphous Ni₃C catalyst structure. With the aid of the mobile nickel atoms, inner layer carbon atoms precipitated rapidly out of the surface and then formed polyynes and Y-junctions. The frequent sinusoidal-like vibration of the branched carbon configurations led to the formation of nascent graphene precursors. In light of the rapid decomposition of the crystalline Ni₃C, it is proposed that the crystalline Ni₃C is unlikely to be a reaction intermediate in the CVD-growth of graphene at high temperatures. However, results present here indicate that Ni₃C films can be employed as precursors in the synthesis of graphene with exciting possibility.

Graphene, a two-dimensional, single-layer sheet of sp²-hybridized carbon atoms, has attracted world-wide attention and research interest, owing to its exceptional physical properties, such as high electronic conductivity, good thermal conductivity, and excellent mechanical strength^{1–3}. The past few years have witnessed considerable progress in the scalable, economical growth of graphene, stimulated by its wide potential applications^{2–4}. Currently, chemical vapor deposition (CVD) using transition or noble metal catalysts, is the preferred method for high-quality graphene synthesis, due to the scalability and cost-effectiveness of the CVD process^{5,6}.

Among the substrates used in the CVD process, Cu^{7,8} and Ni^{9–12} have attracted particular attention with contrasting growth properties. In the former case, low carbon solubility of copper leads to self-limiting surface growth and the formation of monolayer graphene without a bulk reservoir effect^{7,13}. However, the excessive CVD temperature needed for graphene growth, about 1000 °C¹³, results in sublimation of the copper substrate. The as-grown graphene usually displays multiple imperfections such as wrinkles and grain boundaries, due to the weak interaction between graphene and copper¹⁴. On the other hand, nickel has been found to be a common catalyst for the synthesis of graphitic nanostructures^{5,15}. Given the fact that the lattice constant of the Ni(111) surface closely matches that of graphene and the strong interaction between nickel and carbon^{16,17}, nickel was considered to be ideal for epitaxial growth of large homogeneous domains of graphene. Furthermore, the small decomposition barriers of hydrocarbon on Ni and the easy etch of Ni substrate to obtain isolate carbon layer ensure that graphene CVD growth on Ni is one of the promising routes for the synthesis of large-scale graphene^{12,18}.

¹State Key Laboratory of Rare Earth Resource Utilization, Changchun Institute of Applied Chemistry, Chinese Academy of Sciences, Changchun 130022, People's Republic of China. ²University of Chinese Academy of Sciences, Beijing 100049, People's Republic of China. ³Discipline of Chemistry, School of Environmental and Life Sciences, The University of Newcastle, Callaghan 2308, Australia. ⁴Fukui Institute for Fundamental Chemistry, Kyoto University, Kyoto, 606-8103, Japan. Correspondence and requests for materials should be addressed to Y.W. (email: ywang_2012@ciac.ac.cn) or Z.W. (email: zjwu@ciac.ac.cn)

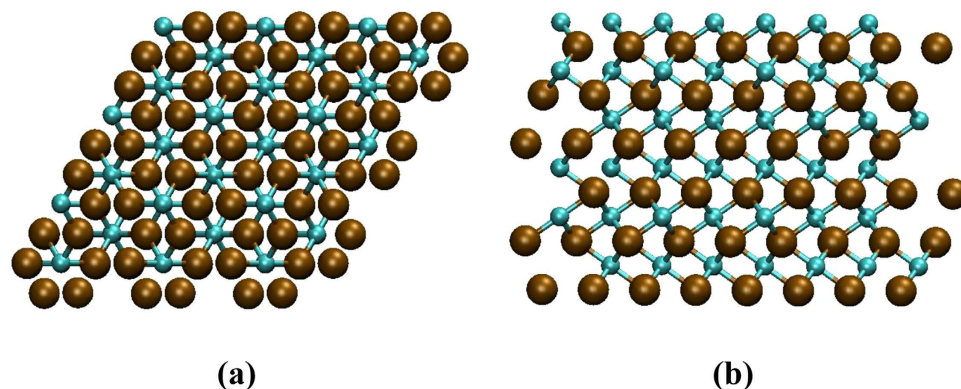


Figure 1. The initial geometry of the crystalline Ni_3C . (a) the top view, (b) the side view. Brown and cyan spheres represent Ni and C atoms, respectively.

Previous studies demonstrated that the following steps are involved in the graphene growth process on Ni-based catalysts: (1) gaseous hydrocarbons are adsorbed and decompose on nickel surfaces; (2) carbon adatoms dissolve into the subsurface or bulk nickel; (3) carbon atoms precipitate back to the nickel surface at low temperature and graphene is formed^{12,13}. However, the relatively high solubility of carbon in Ni and the resulting bulk reservoir effect¹³ make graphene uniformity and layer control with large areas be a very challenging task on Ni. Recent years have evidenced progress in this aspect. The thickness of catalyst, feedstock concentration, substrate cooling rate and the reaction temperature can be adjusted to make graphene growth on Ni controllable^{19–22}. Nevertheless, growth control remains elusive, despite extensive experimental and theoretical studies aimed at elucidating the graphene growth mechanism^{11,12,23–25}. Significant disparities, however, remain in the scientific communities, particularly with respect to whether the formation of nickel carbide is related to the graphene growth. On one hand, Hofmann *et al.* concluded that bulk crystalline Ni carbide is not present during graphene growth^{26,27}. On the other hand, metallurgical studies demonstrated the formation of metastable nickel carbide, due to the high carbon solubility of Ni, contributes to the carbon precipitation from Ni²⁸. Indeed, metastable nickel carbide has been suggested as an intermediate catalyst phase in graphene growth^{9–11,29} and also in carbon nanotube synthesis³⁰. Experimental evidence for the transformation between Ni_3C and graphene was provided by Cao *et al.*³¹. Very recently, a layer of graphene has been observed to precipitate from the Ni_3C phase accompanied by the decomposition of Ni_3C , further indicating that Ni_3C plays an important role during the formation of graphene on nickel catalysts³².

In this study, we present quantum chemical molecular dynamics (QM/MD) simulations of graphene nucleation from crystalline Ni_3C phase. In doing so, we will reveal the atomistic mechanism of this non-equilibrium process and elucidate the relationship between the nucleation of graphene and the crystalline Ni_3C phase at high temperature.

Results

The mechanism of graphene nucleation. The model structure studied in this work is shown in Fig. 1. For details, see Methods section. The snapshots of representative trajectories, i.e., trajectory 3 and trajectory 5, following 200 ps of graphene nucleation simulation, are shown in Fig. 2. They are also detailed in Supplementary Movie S1–S2, respectively. The final structures of trajectories 1–10 are depicted in Supplementary Fig. S1.

It can be seen from Supplementary Movies S1 and S2 that subsurface carbon atoms precipitate out of the catalyst surface at the very beginning of the simulation. Once carbon atoms were separated out, they underwent subsequent diffusion over the nickel surface, which was facilitated by the relatively weak Ni–C interaction compared to C–C interaction. As a natural consequence of the diffusion, the small C_n units gradually coalesced with each other to form extended polyene chains and Y-junctions, which are the prerequisite for the formation of the carbon network. Meanwhile, the Mermin free energy³³ of the Ni_3C system drops substantially by *ca.* 3.0 eV per Ni_3C unit, due to repeated C–C bond formation, making the entire system to be more stable. This minimization of free energy is the driving force for carbon diffusion from bulk Ni_3C substrate, which is in line with the observations of carbon nanofiber growth³⁴.

Figure 2a shows the details of the nucleation process observed in trajectory 3. A complex Y-junction attached with some shorter linear C_n chains was formed at 16.0 ps. A hexagon was formed preferentially after *ca.* 20 ps, which is different from “pentagon-first” mechanism that is usually observed during graphene and carbon nanotube nucleation^{23,24}. This may be attributed to the role played by the exterior nickel atom that is highlighted by a yellow arrow in Fig. 2a, which indicates the auxiliary effect of the nickel catalyst during the graphene nucleation process. This point will be discussed in further detail below. As growth continued, this structure incorporated more C atoms and shorter C_n chains branching out from the original hexagon, and additional graphene rings were added to the nucleus (at 47.2 ps). It is

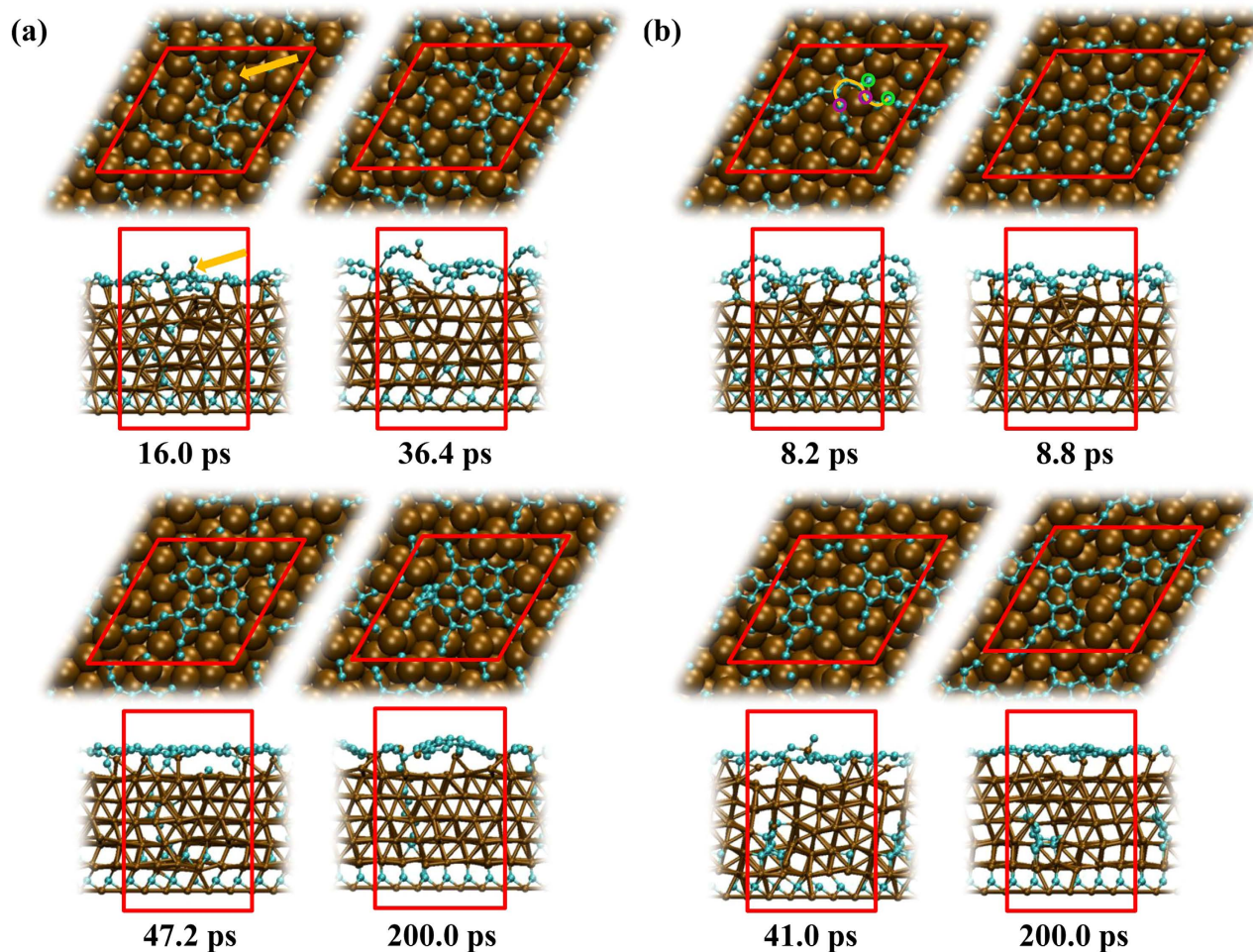


Figure 2. Evolution of graphene nucleation at 1180 K from crystalline Ni₃C at different simulation time at both top and side views. (a) trajectory 3, (b) trajectory 5. Color convention is the same as Figure 1. The location of the periodic boundary is indicated by the red line. A surface nickel atom in (a) is highlighted by a yellow arrow. The polyyn chain, which exhibited sinusoidal-like vibration in (b), is highlighted in yellow line. The two pairs of the bonding carbon atoms in (b) are highlighted in purple and green circle, respectively.

noted that the sp²-hybridized structure remained flat throughout this process. Three pentagons and two hexagons were generated sequentially in the immediate vicinity of the original hexagon by the end of the simulation time (at 200 ps). A geometry analogous to the core-shell structured C₂₁, which was found to be the precursor in the initial graphene CVD growth³⁵, was formed. This precursor became dome-like simultaneously, stabilized by the interaction between its edge carbon atoms and adjacent nickel atoms. This result is consistent with the previous observations^{35–37}. An analogous structure was also observed in trajectory 7 (Supplementary Fig. S1).

We will now turn to discuss the reaction observed in trajectory 5 (Fig. 2b), as it shows features more typical, but different from, the mechanism of graphene nucleation in trajectory 3. The rapid precipitation of subsurface carbon atoms and the subsequent formation of polyyn chains preceded the emergence of the “Y-junction” structure, consistent with the aforementioned mechanism. The first sp²-carbon polygon driven by the sinusoidal-like vibration of the polyyn chains (highlighted by the yellow line in Fig. 2b), however, became a pentagon under this circumstance at 8.6 ps (Supplementary Movie S2). Carbon nanotube growth shows similar behavior³⁸. Following the formation of the first pentagon, the second pentagon was formed immediately through the quick connection between the remaining polyyn chains and the carbon atom extended from adjacent pentagon sites. The two pairs of bonding carbon atoms are highlighted in purple and green circle in Fig. 2b, respectively. This resulted in the formation of a fused pentagon pair (8.8 ps in Fig. 2b), which was anchored to the nickel particles by the carbon branches. Once created, the pentagon-pentagon pair was rather stable and could survive throughout the simulation process. Another fused pentagon pair was formed subsequently (41.0 ps). It is evident that the formation of fused pentagon pairs is a prominent feature of this system (see the snapshots of trajectory 1, 5, 8, 9

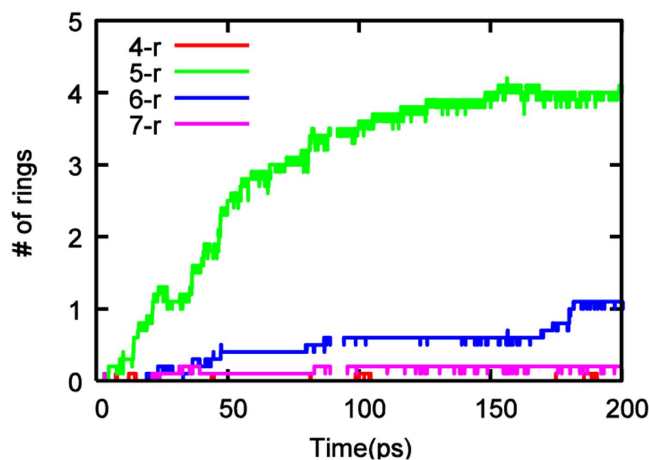


Figure 3. Average polygonal carbon ring populations formed during graphene nucleation from crystalline Ni_3C .

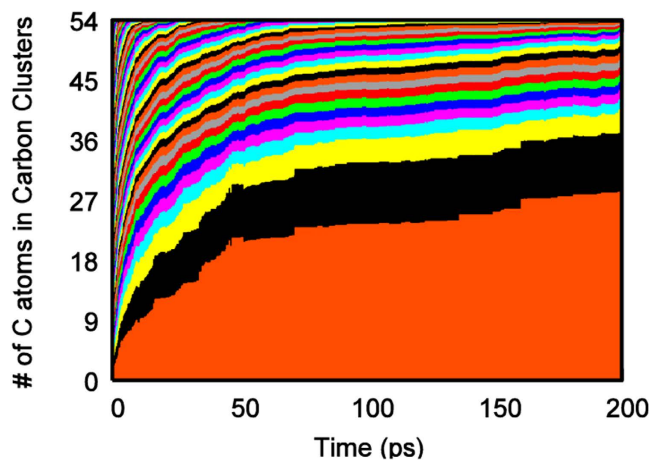


Figure 4. Carbon cluster size ($\#C_{\text{cluster}}$) evolution in crystalline Ni_3C as a function of simulation time. Each color indicates a unique carbon cluster observed during the simulation. The way in which the sizes of these colored areas change indicates how these cluster sizes change. In each case, the largest cluster grows by consuming smaller fragments. All data were averaged over 10 trajectories.

and 10 in Supplementary Fig. S1). This result is somewhat unexpected, as it clearly violated the so-called isolated pentagon rule (IPR)³⁹, and indicates that this process does not proceed via the most thermodynamically stable pathway. Instead, fused pentagon defects, once formed, become kinetically trapped in the growing graphene structure, and are presumably healed over longer timescales^{40,41}.

Figure 3 displays the time evolution of the number of polygon rings during graphene nucleation from crystalline Ni_3C system, averaged over the ten trajectories. Ring populations of individual trajectory 1–10 are provided in Supplementary Fig. S2. Because the inherent instability of four- and three-membered rings, their formation in the process of graphene nucleation was transitory, and insignificant with respect to the graphene nucleation mechanism. For pentagons, it is found that their numbers increased drastically right after the starting of the simulation process and became the predominant polygon. This is in accordance with the observation of the formation of fused pentagon structures in most of the ten trajectories. The formation of hexagon experienced an induction period and its numbers increased quite slowly with the simulation process. Heptagons were seldom observed, in line with our previous studies in which subsurface carbon atoms segregated out to nucleate a graphene precursor^{25,42}. It is evidently more favourable for the underlying catalyst structure to be deformed under these conditions, thereby supporting the positively-curved, pentagon-rich structure through Ni-C σ bonding.

The variation in the population of polygons during the simulation process in Fig. 3 is reflected in Fig. 4 accordingly, which shows the time evolution of each individual carbon cluster, averaged in 10 trajectories in terms of size. The applied threshold value for C-C bond lengths is 1.75 Å. The largest cluster grew rapidly in the first 50 ps during which the number of polygons, especially the pentagon, increased

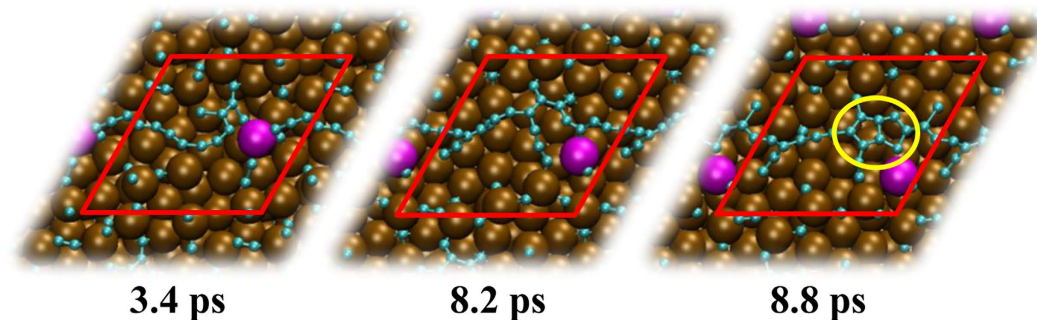


Figure 5. The coalescence of polyynic chains and the subsequent ring condensation observed in trajectory 5 at different simulation time. Color convention is the same as Figure 1. The nickel atom that connects polyynic chains is highlighted in purple. The fused pentagon pair is highlighted in a yellow circle.

promptly (Fig. 3). During this time, the number of the other smaller clusters decreased simultaneously to form large cluster. In the subsequent 150 ps, the increase of polygon slowed down and then reached equilibrium gradually, confirmed by the synchronized change in the size of all the clusters.

The role of the nickel catalyst. Given the larger strength of C-Ni bond versus that of Ni-Ni bond⁴³, nickel layers in Ni₃C lattice were restricted by the carbon atoms to stay between them to some extent. With the segregation of subsurface carbon atoms, the distance between nickel layers became larger initially, as shown in Supplementary Movie S1–S2. The Ni₃C lattice was relaxed and damaged rapidly, resulting in a catalyst structure resembled an amorphous Ni₃C phase. The destruction of the crystalline Ni₃C structure warranted the high mobility of nickel atoms in the subsequent process, which was visualized clearly in Supplementary Movie S1–S2.

With the continuous precipitation of carbon, many nickel atoms were also pulled out. This phenomenon favored the subsequent precipitation of the inner layer carbon atoms by providing larger interspace. On the other hand, the Ni-C_n-Ni bridge configurations were frequently found to stabilize the polyynic chains on the nickel surface via terminal Ni-C σ bonds. This is consistent with the observation in previous studies^{25,42,44}. Once on the surface, carbon atoms showed high mobility, in spite of obstruction of surface nickel atoms. However, with the connection of carbon atoms on nickel surface, the coalescence of polyynic chains would be subject to a high-energy barrier, due to the obstructive motion of the surface nickel atoms. Interestingly, the coalescence of polyynic chains appeared frequently, ultimately forming carbon networks in the present situation. This is attributed to the mobility of nickel atoms. Figure 5 depicts this process occurring in trajectory 5. Different kinds of C_n structures were connected by a single nickel atom on surface at 3.4 ps. Then the nickel atom acted as a “needle”, stitching them together, making them drift on the nickel surface (see the snapshot at 8.2 ps). This is similar to the graphene hole-healing process⁴⁵. Afterwards, the generated branched carbon configurations were less mobile, and coalesced among them by frequent fluctuation. This is understandable, since the branched configurations of carbon have substantial energy barrier for movement even on low-defect nickel surface⁴⁶. As discussed above, fused pentagons were formed promptly (see the snapshot at 8.8 ps). With the formation of carbon networks, the ordering of underlying nickel layers was restored to an extent (Supplementary Fig. S1).

Comparison between graphene nucleation from crystalline and amorphous Ni₃C. The evolution of the number of polygons and the size of carbon clusters during the QM/MD simulations were the product of the movement of carbon atoms in the Ni₃C system. Figure 6 depicts the variation in the ratios of subsurface and surface carbon to the total carbon, as a function of time in crystalline Ni₃C and amorphous Ni₃C systems, respectively. These processes are similar in the changing trend of the ratio of carbon atoms, i.e., a drastic increase in the ratio of surface carbon atoms was accompanied by a simultaneous decrease in the ratio of subsurface carbon atoms. In addition, their equilibrium was reached much earlier (Fig. 6) than that of the number of polygons and the size of carbon clusters (Figs 3 and 4). This indicates that after precipitation on nickel catalysts, different kinds of C_n clusters coalesce and contribute to the nucleation of graphene precursor. In light of the rapid decomposition of the crystalline Ni₃C upon thermal annealing, it is safe to deduce that crystalline nickel carbide is not the reaction intermediate in the CVD-growth of graphene at high temperature. Crystalline nickel carbide observed in experiments^{31,32} may be ascribed to graphene production being stopped under the rapid cooling process.

However, the variation of surface carbon atoms increases more slowly in crystalline Ni₃C compared with the amorphous one. This conclusion is further corroborated by the obtained Lindemann index, δ , for both systems in Fig. 7. It is typically accepted that $\delta = 0.1$ marks the transition between the solid and liquid phases⁴⁷. Figure 7 shows that crystalline and amorphous Ni₃C catalysts rapidly undergo a solid to liquid-like phase transition upon thermal annealing, as indicated by the rapid increase of δ in both systems. Thus, the atoms in both systems would show high mobility. Nonetheless, the formation of C-C

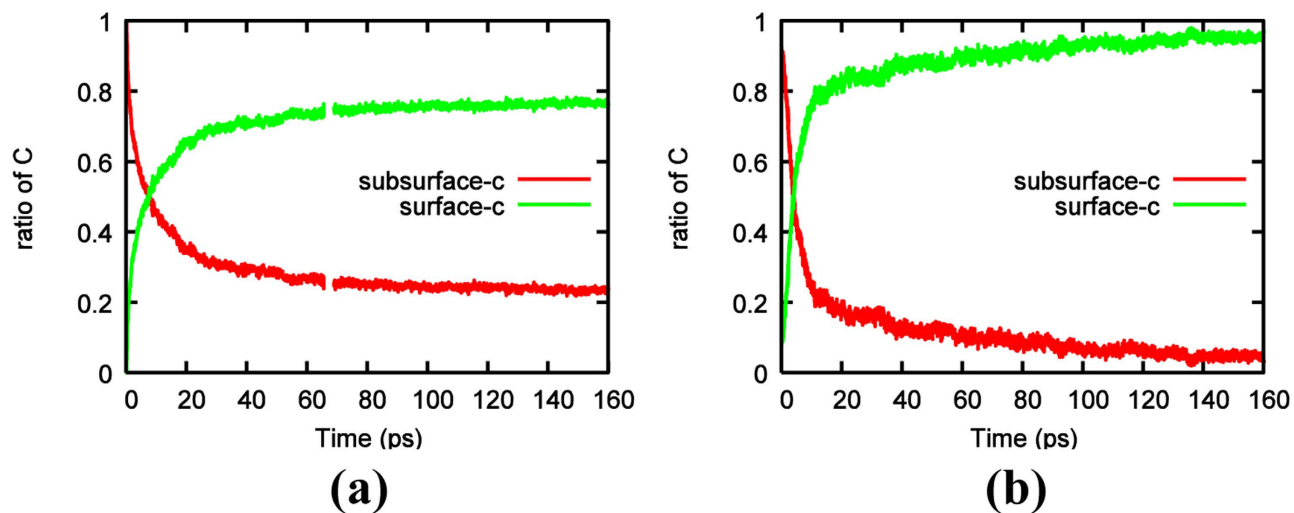


Figure 6. Ratios of subsurface-C/total carbon atoms and surface-C/total carbon atoms as a function of time for (a) crystalline Ni_3C and (b) amorphous Ni_3C^{42} , respectively. All data were averaged over 10 trajectories.

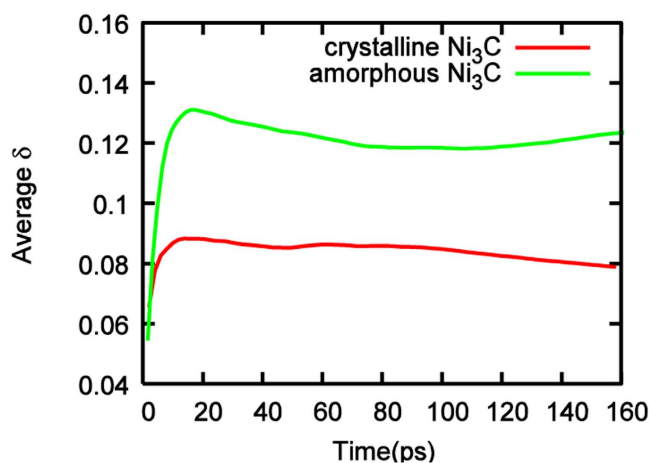


Figure 7. δ values of crystalline and amorphous Ni_3C at 1180 K. All data averaged over 10 trajectories.

bonds and subsequently the sp^2 -hybridized carbon network on the nickel surface, in part, “solidifies” the system. This can be confirmed by the gradual decrease of the average δ in both systems after the initial peak. The smaller δ for the crystalline Ni_3C catalyst indicates a more solid-like character that is likely to impede carbon precipitation and graphene nucleation, compared to the amorphous catalyst.

Within the deeper layers of the crystalline Ni_3C catalyst, carbon diffusion is slower, presumably due to the greater confining effects of the nickel layers. Under these conditions this subsurface carbon is potentially more likely to gather into subsurface clusters that remain within the catalyst (Supplementary Fig. S1), and do not contribute to the nucleation of nascent graphene precursor. As a result, a carbon-free nickel subsurface layer was embedded in between graphene precursors and bulk nickel carbide (Fig. 8), which has also been found in previous studies^{11,29}. This phenomenon is different from the previous amorphous Ni_3C simulation, in which Ni is substituted by C and less layers are selected⁴². This makes the ratio of surface carbon atoms in amorphous Ni_3C system be larger than that in crystalline one during the simulation process (Fig. 6). This result is also different from the graphene growth starting from elemental Ni catalyst where carbon atoms are added constantly in bulk Ni^{25} and the subsurface carbon clusters precipitate out once reach a certain size. This is because in this study, there is no continual supplement to the inner layer carbon atoms and the subsurface clusters are difficult to segregate out. Therefore, higher subsurface carbon densities are necessary to assist the precipitation of subsurface clusters and the nucleation of ordered graphene precursor on the surface^{25,42,43}.

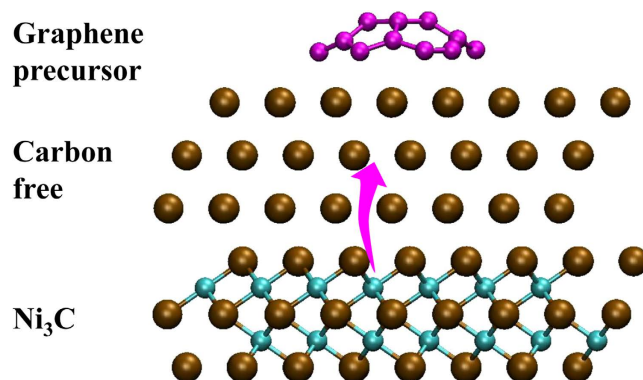


Figure 8. Schematic of graphene growth process from crystalline Ni_3C . Brown spheres represent Ni atoms. Carbon atoms in deep layer and in nascent graphene precursor are colored in cyan and purple, respectively. Purple arrow indicates the movement (supply) of subsurface carbon atoms.

These results suggest that crystalline Ni_3C , which includes both carbon source and catalyst, potentially enables facile, controlled graphene synthesis via carbon precipitation. In the initial stage of graphene nucleation, crystalline Ni_3C can provide carbon source continually. The graphene precursor can be formed by the precipitation of shallow subsurface carbon during the early stages of thermal annealing, as discussed above, which leads to the formation of a carbon-free nickel layer. Subsequently, deeper carbon layers can potentially migrate to this carbon-free nickel layer, which is a thermodynamically controlled process and higher temperature is required (indicated by the purple arrow, Fig. 8). In principle, this process can be repeated continually, opening up the exciting possibility for graphene fabrication by controlling the Ni_3C thickness and/or the diffusion rate of subsurface carbon atoms.

Discussion

Graphene nucleation from model crystalline Ni_3C catalyst surfaces has been studied using QM/MD simulations. The results indicated that the lattice of Ni_3C was quickly relaxed and damaged upon thermal annealing, resulting in a catalyst structure resembled an amorphous Ni_3C phase. Inner layer carbon atoms experienced rapid precipitation and subsequent formation of polyene chains due to the stronger C-C interaction compared with C-Ni interaction. The mobility of nickel atoms played a critical role during the nucleation process. On one hand, it is beneficial to the rapid precipitation of carbon atoms; on the other hand, it enables surface nickel atoms facilitate the coalescence of surface-adsorbed polyene chains, thereby stabilizing the generated Y-junctions. The frequent sinusoidal-like vibrations of the branched carbon configurations made themselves coalesce to form nascent graphene precursor.

In light of the rapid decomposition of the crystalline Ni_3C upon thermal annealing, we can deduce that crystalline nickel carbide is not the reaction intermediate in the CVD-growth of graphene at high temperature. Crystalline nickel carbide phases, observed experimentally, may be recovered under the rapid cooling process after the graphene production is stopped. However, this opens up the exciting possibility for experimentalists to fabricate graphene by a proper thickness of Ni_3C precursor.

Methods

Graphene nucleation has been investigated in this work with nonequilibrium QM/MD simulations based on the self-consistent charge density functional tight-binding (SCC-DFTB) method⁴⁸. The standard trans 3d-0-1⁴⁹ and mio-0-1⁴⁸ parameter sets were employed. This approach consists of integrating the classical equations of motion, in conjunction with a quantum chemical potential. The nuclear equations of motion were integrated using the Velocity Verlet algorithm⁵⁰ ($\Delta t = 1$ fs), with the NVT ensemble being maintained via a Nosé-Hoover chain thermostat⁵¹ (chain-length 3) connected to the degrees of freedom of the system. The nuclear temperature was maintained at 1180 K throughout all simulations, which is the temperature usually employed in experiments^{13,17}. The quantum chemical potential was evaluated “on-the-fly” at each MD iteration using the SCC-DFTB method, as implemented in the DFTB + program⁵². A finite electronic temperature of 3000 K was enforced throughout all simulations, and so orbital occupations for molecular orbitals near the Fermi energy level were described by a Fermi-Dirac distribution function (and could vary continuously over the interval $[0, 2]$)³³. The use of a finite electronic-temperature approach alleviated SCC convergence issue, which is from the presence of many near-degenerate Ni d orbitals and unterminated, dangling, C atoms. In such a case, the variational SCC-DFTB energy becomes the Mermin free energy³³, defined as follows,

$$f_i = \frac{1}{\exp[(\varepsilon_i - \mu)/k_B T_e] + 1} \quad (1)$$

$$S_e = -2k_B \sum_i^{\infty} f_i \ln f_i + (1 - f_i) \ln(1 - f_i) \quad (2)$$

$$E_{mermin} = E_{tot} - T_e S_e \quad (3)$$

where T_e is the electronic temperature, f_i is the fractional occupation numbers of Kohn-Sham eigenstates ($0 \leq f_i \leq 1$), and S_e is electronic entropy, respectively. This method has been previously applied extensively in the investigations of carbon nanostructure growth^{23–25,42}.

To our knowledge, two polymorphs of Ni_3C have been proposed: orthorhombic and hexagonal structures^{53–56}. Previous theoretical studies indicated that the orthorhombic structure is 0.157 eV higher in energy than the hexagonal one per Ni_3C unit, which was corroborated by experimental observation of the existence of only hexagonal Ni_3C ^{53,54}. Thus, the hexagonal structure of Ni_3C with the lattice parameter of $a = 4.553 \text{ \AA}$ and $c = 12.92 \text{ \AA}$ was used in this work^{55,56}. In the hexagonal structure, the octahedral interstices of nickel atoms are slightly deformed, one-third of which is occupied by carbon atoms. Nickel layers alternate with carbon layers for Ni_3C (001) surface to form the nuclei of hexagonal Ni_3C phase. For the QM/MD simulations, a 3×3 supercell consisting of $Ni_{162}C_{54}$ was employed (Fig. 1). The last layer of Ni atoms and carbon atoms in this model were frozen throughout all simulations, as an approximation to the bulk region. Periodic boundary conditions were enforced using the Γ point approximation, and a vacuum region of 10 nm was applied to avoid interactions between adjacent surfaces. The initial structure, as shown in Fig. 1, was optimized. Then ten independent trajectories were calculated based on the randomized initial velocities, which satisfied a Maxwell–Boltzmann distribution corresponding to 1180 K, for the subsequent graphene growth. These trajectories are denoted using the number 1–10.

The Lindemann index, δ ⁵⁷, which was defined in equation (4), was employed here to analyze the physical state of Ni_3C catalyst.

$$\delta = \frac{1}{N(N-1)} \sum_{i < j} \frac{\sqrt{\langle r_{ij}^2 \rangle_T - \langle r_{ij} \rangle_T^2}}{\langle r_{ij} \rangle_T} \quad (4)$$

where N is the number of atoms in the relevant system, r_{ij} is the instantaneous distance between atoms i and j , and the brackets denote thermal averaging over a finite interval of time. The Lindemann index has been used on a number of occasions to elucidate the phase-transitions in transition metal and transition metal carbide nanoparticles, in the context of carbon nanotube nucleation and growth^{58–60}.

References

- Lee, C., Wei, X., Kysar, J. W. & Hone, J. Measurement of the elastic properties and intrinsic strength of monolayer graphene. *Science* **321**, 385–388 (2008).
- Geim, A. K. & Novoselov, K. S. The rise of graphene. *Nat. Mater.* **6**, 183–191 (2007).
- Balandin, A. A. *et al.* Superior thermal conductivity of single-layer graphene. *Nano Lett.* **8**, 902–907 (2008).
- Vivekchand, S. R. C., Rout, C., Subrahmanyam, K. S., Govindaraj, A. & Rao, C. N. R. Graphene-based electrochemical supercapacitors. *J. Chem. Sci.* **120**, 9–13 (2008).
- Kim, K. S. *et al.* Large-scale pattern growth of graphene films for stretchable transparent electrodes. *Nature* **457**, 706–710 (2009).
- Reina, A. *et al.* Large area, few-layer graphene films on arbitrary substrates by chemical vapor deposition. *Nano Lett.* **9**, 30–35 (2009).
- Li, X. *et al.* Large-area synthesis of high-quality and uniform graphene films on copper foils. *Science* **324**, 1312–1314 (2009).
- Fan, Y., He, K., Tan, H., Speller, S. & Warner, J. H. Crack-free growth and transfer of continuous monolayer graphene grown on melted copper. *Chem. Mater.* **26**, 4984–4991 (2014).
- Jacobson, P. *et al.* Nickel carbide as a source of grain rotation in epitaxial graphene. *ACS Nano* **6**, 3564–3572 (2012).
- Lahiri, J., Miller, T., Adamska, L., Oleynik, I. I. & Batzill, M. Graphene growth on Ni(111) by transformation of a surface carbide. *Nano Lett.* **11**, 518–522 (2010).
- Weatherup, R. S. *et al.* Interdependency of subsurface carbon distribution and graphene–catalyst interaction. *J. Am. Chem. Soc.* **136**, 13698–13708 (2014).
- Patera, L. L. *et al.* *In situ* observations of the atomistic mechanisms of Ni catalyzed low temperature graphene growth. *ACS Nano* **7**, 7901–7912 (2013).
- Li, X., Cai, W., Colombo, L. & Ruoff, R. S. Evolution of graphene growth on Ni and Cu by carbon isotope labeling. *Nano Lett.* **9**, 4268–4272 (2009).
- Gao, L., Guest, J. R. & Guisinger, N. P. Epitaxial graphene on Cu(111). *Nano Lett.* **10**, 3512–3516 (2010).
- Moors, M. *et al.* Early stages in the nucleation process of carbon nanotubes. *ACS Nano* **3**, 511–516 (2009).
- Kozlov, S. M., Viñes, F. & Görling, A. Bonding mechanisms of graphene on metal surfaces. *J. Phys. Chem. C* **116**, 7360–7366 (2012).
- Shelton, J. C., Patil, H. R. & Blakely, J. M. Equilibrium segregation of carbon to a nickel(111) surface: A surface phase transition. *Surf. Sci.* **43**, 493–520 (1974).
- Bianchini, F., Patera, L. L., Peressi, M., Africh, C. & Comelli, G. Atomic scale identification of coexisting graphene structures on Ni(111). *J. Phys. Chem. L* **5**, 467–473 (2014).
- Batzill, M. The surface science of graphene: Metal interfaces, CVD synthesis, nanoribbons, chemical modifications, and defects. *Surf. Sci. Rep.* **67**, 83–115 (2012).
- Reina, A. *et al.* Growth of large-area single- and bi-layer graphene by controlled carbon precipitation on polycrystalline Ni surfaces. *Nano Res.* **2**, 509–516 (2009).

21. Addou, R., Dahal, A., Sutter, P. & Batzill, M. Monolayer graphene growth on Ni(111) by low temperature chemical vapor deposition. *Appl. Phys. Lett.* **100**, 021601–021603 (2012).
22. Weatherup, R. S., Dlubak, B. & Hofmann, S. Kinetic control of catalytic CVD for high-quality graphene at low temperatures. *ACS Nano* **6**, 9996–10003 (2012).
23. Wang, Y. *et al.* Template effect in the competition between haecelite and graphene growth on Ni(111): Quantum chemical molecular dynamics simulations. *J. Am. Chem. Soc.* **133**, 18837–18842 (2011).
24. Page, A. J., Wang, Y., Li, H.-B., Irle, S. & Morokuma, K. Nucleation of graphene precursors on transition metal surfaces: Insights from theoretical simulations. *J. Phys. Chem. C* **117**, 14858–14864 (2013).
25. Wang, Y. *et al.* Step-edge self-assembly during graphene nucleation on a nickel surface: QM/MD simulations. *Nanoscale* **6**, 140–144 (2014).
26. Weatherup, R. S. *et al.* *In situ* characterization of alloy catalysts for low-temperature graphene growth. *Nano Lett.* **11**, 4154–4160 (2011).
27. Weatherup, R. S. *et al.* On the mechanisms of Ni-catalysed graphene chemical vapour deposition. *ChemPhysChem* **13**, 2544–2549 (2012).
28. Mattevi, C., Kim, H. & Chhowalla, M. A review of chemical vapour deposition of graphene on copper. *J. Mater. Chem.* **21**, 3324–3334 (2011).
29. Benayad, A. & Li, X.-S. Carbon free nickel subsurface layer tessellating graphene on Ni(111) surface. *J. Phys. Chem. C* **117**, 4727–4733 (2013).
30. Achour, A. *et al.* Carbon nanotube growth at 420 °C using nickel/carbon composite thin films as catalyst supports. *Diamond Relat. Mater.* **34**, 76–83 (2013).
31. Cao, Y., Su, Q., Che, R., Du, G. & Xu, B. One-step chemical vapor synthesis of Ni/graphene nanocomposites with excellent electromagnetic and electrocatalytic properties. *Synth. Met.* **162**, 968–973 (2012).
32. Xiong, W. *et al.* Single-step formation of graphene on dielectric surfaces. *Adv. Mater.* **25**, 630–634 (2013).
33. Wentzcovitch, R. M., Martins, J. L. & Allen, P. B. Energy versus free-energy conservation in first-principles molecular dynamics. *Phys. Rev. B* **45**, 11372–11374 (1992).
34. Zhu, Y.-A., Dai, Y.-C., Chen, D. & Yuan, W.-K. First-principles study of carbon diffusion in bulk nickel during the growth of fishbone-type carbon nanofibers. *Carbon* **45**, 21–27 (2007).
35. Yuan, Q. *et al.* Magic carbon clusters in the chemical vapor deposition growth of graphene. *J. Am. Chem. Soc.* **134**, 2970–2975 (2012).
36. Wang, B., Ma, X., Caffio, M., Schaub, R. & Li, W.-X. Size-selective carbon nanoclusters as precursors to the growth of epitaxial graphene. *Nano Lett.* **11**, 424–430 (2011).
37. Lacovig, P. *et al.* Growth of dome-shaped carbon nanoislands on Ir(111): The intermediate between carbidic clusters and quasi-free-standing graphene. *Phys. Rev. Lett.* **103**, 166101 (2009).
38. Ohta, Y., Okamoto, Y., Page, A. J., Irle, S. & Morokuma, K. Quantum chemical molecular dynamics simulation of single-walled carbon nanotube cap nucleation on an iron particle. *ACS Nano* **3**, 3413–3420 (2009).
39. Dinadayalane, T. C. & Sastry, G. N. Isolated pentagon rule in buckybowls: A computational study on thermodynamic stabilities and bowl-to-bowl inversion barriers. *Tetrahedron* **59**, 8347–8351 (2003).
40. Page, A. J., Ohta, Y., Okamoto, Y., Irle, S. & Morokuma, K. Defect healing during single-walled carbon nanotube growth: A density-functional tight-binding molecular dynamics investigation. *J. Phys. Chem. C* **113**, 20198–20207 (2009).
41. Li, H.-B. *et al.* Graphene nucleation on a surface-molten copper catalyst: Quantum chemical molecular dynamics simulations. *Chem. Sci.* **5**, 3493–3500 (2014).
42. Jiao, M. *et al.* Graphene nucleation from amorphous nickel carbides: QM/MD studies on the role of subsurface carbon density. *J. Phys. Chem. C* **118**, 11078–11084 (2014).
43. Li, H.-B., Page, A. J., Wang, Y., Irle, S. & Morokuma, K. Sub-surface nucleation of graphene precursors near a Ni(111) step-edge. *Chem. Commun.* **48**, 7937–7939 (2012).
44. Wu, P., Zhang, W., Li, Z., Yang, J. & Hou, J. G. Communication: Coalescence of carbon atoms on Cu (111) surface: Emergence of a stable bridging-metal structure motif. *J. Chem. Phys.* **133**, 071101 (2010).
45. Meng, L., Jiang, J., Wang, J. & Ding, F. Mechanism of metal catalyzed healing of large structural defects in graphene. *J. Phys. Chem. C* **118**, 720–724 (2013).
46. Cheng, D., Barcaro, G., Charlier, J.-C., Hou, M. & Fortunelli, A. Homogeneous nucleation of graphitic nanostructures from carbon chains on Ni(111). *J. Phys. Chem. C* **115**, 10537–10543 (2011).
47. Zhou, Y., Karplus, M., Ball, K. D. & Berry, R. S. The distance fluctuation criterion for melting: Comparison of square-well and morse potential models for clusters and homopolymers. *J. Chem. Phys.* **116**, 2323–2329 (2002).
48. Elstner, M. *et al.* Self-consistent-charge density-functional tight-binding method for simulations of complex materials properties. *Phys. Rev. B* **58**, 7260–7268 (1998).
49. Zheng, G. *et al.* Parameter calibration of transition-metal elements for the spin-polarized self-consistent-charge density-functional tight-binding (DFTB) Method: Sc, Ti, Fe, Co, and Ni. *J. Chem. Theory Comput.* **3**, 1349–1367 (2007).
50. Swope, W. C., Andersen, H. C., Berens, P. H. & Wilson, K. R. A computer simulation method for the calculation of equilibrium constants for the formation of physical clusters of molecules: Application to small water clusters. *J. Chem. Phys.* **76**, 637–649 (1982).
51. Martyna, G. J., Klein, M. L. & Tuckerman, M. Nosé–Hoover chains: the canonical ensemble via continuous dynamics. *J. Chem. Phys.* **97**, 2635–2643 (1992).
52. Aradi, B., Hourahine, B. & Frauenheim, T. DFTB+, a sparse matrix-based implementation of the DFTB method. *J. Phys. Chem. A* **111**, 5678–5684 (2007).
53. Hwang, J. Y. *et al.* Templated growth of hexagonal nickel carbide nanocrystals on vertically aligned carbon nanotubes. *J. Phys. Chem. C* **114**, 10424–10429 (2010).
54. Gibson, J. S., Uddin, J., Cundari, T. R., Bodiford, N. K. & Wilson, A. K. First-principle study of structure and stability of nickel carbides. *J. Phys. Condens. Matter* **22**, 445503 (2010).
55. Nagakura, S. Study of metallic carbides by electron diffraction part II. Crystal structure analysis of nickel carbide. *J. Phys. Soc. Jpn.* **13**, 1005–1014 (1958).
56. Yue, L., Sabiryanov, R., Kirkpatrick, E. M. & Leslie-Pelecky, D. L. Magnetic properties of disordered Ni₃C. *Phys. Rev. B* **62**, 8969–8975 (2000).
57. Lindemann, F. A. The calculation of molecular natural frequencies. *Phys. Z.* **11**, 609–612 (1910).
58. Shibuta, Y. & Maruyama, S. A molecular dynamics study of the effect of a substrate on catalytic metal clusters in nucleation process of single-walled carbon nanotubes. *Chem. Phys. Lett.* **437**, 218–223 (2007).
59. Page, A. J., Yamane, H., Ohta, Y., Irle, S. & Morokuma, K. QM/MD simulation of SWNT nucleation on transition-metal carbide nanoparticles. *J. Am. Chem. Soc.* **132**, 15699–15707 (2010).
60. Ding, F., Rosén, A., Curtarolo, S. & Bolton, K. Modeling the melting of supported clusters. *Appl. Phys. Lett.* **88**, 133110 (2006).

Acknowledgements

The authors thank the National Natural Science Foundation of China for financial support (Grant Nos: 21203174, 21221061, 21273219) and the Natural Science Foundation of Jilin Province (Nos. 20130522141JH, 20130101179JC-07). The authors also thank the financial support from Department of Science and Technology of Sichuan Province. AJP acknowledges support from Australian Research Council Discovery Project DP140102894. The computational resource is partly supported by the Performance Computing Center of Jilin University, China. We are also grateful to the Computing Center of Jilin Province for essential support.

Author Contributions

Y.W. and Z.J.W. conceived and coordinated the research. M.G.J. performed theoretical calculations and wrote the manuscript primarily. K.L., W.G., A.J. and K.M. contributed in the discussion of the results. All authors contributed to writing and revising the manuscript.

Additional Information

Supplementary information accompanies this paper at <http://www.nature.com/srep>

Competing financial interests: The authors declare no competing financial interests.

How to cite this article: Jiao, M. *et al.* Crystalline Ni₃C as both carbon source and catalyst for graphene nucleation: a QM/MD study. *Sci. Rep.* **5**, 12091; doi: 10.1038/srep12091 (2015).



This work is licensed under a Creative Commons Attribution 4.0 International License. The images or other third party material in this article are included in the article's Creative Commons license, unless indicated otherwise in the credit line; if the material is not included under the Creative Commons license, users will need to obtain permission from the license holder to reproduce the material. To view a copy of this license, visit <http://creativecommons.org/licenses/by/4.0/>